Rotational flow in tapered slab rocket motors

Tony Saad, Oliver C. Sams IV, and Joseph Majdalani

Citation: Physics of Fluids (1994-present) **18**, 103601 (2006); doi: 10.1063/1.2354193
View online: http://dx.doi.org/10.1063/1.2354193
View Table of Contents: http://scitation.aip.org/content/aip/journal/pof2/18/10?ver=pdfcov
Published by the AIP Publishing

Rotational flow in tapered slab rocket motors

Tony Saad, Oliver C. Sams IV, and Joseph Majdalani[a)]
University of Tennessee Space Institute, Tullahoma, Tennessee 37388

(Received 20 May 2006; accepted 15 August 2006; published online 2 October 2006)

Internal flow modeling is a requisite for obtaining critical parameters in the design and fabrication of modern solid rocket motors. In this work, the analytical formulation of internal flows particular to motors with tapered sidewalls is pursued. The analysis employs the vorticity-streamfunction approach to treat this problem assuming steady, incompressible, inviscid, and nonreactive flow conditions. The resulting solution is rotational following the analyses presented by Culick for a cylindrical motor. In an extension to Culick's work, Clayton has recently managed to incorporate the effect of tapered walls. Here, an approach similar to that of Clayton is applied to a slab motor in which the chamber is modeled as a rectangular channel with tapered sidewalls. The solutions are shown to be reducible, at leading order, to Taylor's inviscid profile in a porous channel. The analysis also captures the generation of vorticity at the surface of the propellant and its transport along the streamlines. It is from the axial pressure gradient that the proper form of the vorticity is ascertained. Regular perturbations are then used to solve the vorticity equation that prescribes the mean flow motion. Subsequently, numerical simulations via a finite volume solver are carried out to gain further confidence in the analytical approximations. In illustrating the effects of the taper on flow conditions, comparisons of total pressure and velocity profiles in tapered and nontapered chambers are entertained. Finally, a comparison with the axisymmetric flow analog is presented. © *2006 American Institute of Physics*. [DOI: 10.1063/1.2354193]

I. INTRODUCTION

In the design of solid rocket motors, internal flowfield modeling is of paramount importance in evaluating the impact of mean flow on unsteady wave motions, estimating acoustic energy, predicting the onset of hydrodynamic instability, and assessing velocity and pressure coupling with propellant burning. Clearly, accurate mathematical modeling of the pressure distribution and velocity profiles is important with respect to the efficient design and manufacture of the structural components that comprise the solid rocket motor (SRM).

Overprediction of the pressure load would result in increased motor fabrication cost and weight which, in turn, would result in a negative impact on motor efficiency. If the pressure load is under-predicted, the potential risks can be significant. Four decades ago, Culick developed a mean flow solution for the internal flowfield of a circular-port SRM using an inviscid, incompressible, and rotational flow model.[1] This profile was used in many studies to predict the pressure variation and combustion instabilities.[2–8] Currently, it is used as a baseline in known ballistic codes such as SSP (Standard Stability Prediction).[9]

Modern SRMs are manufactured with small tapers that reduce the contact between the casting mandrels and the propellant during mandrel removal. The small, divergent angles aid in the reduction of shear stress on the surface of the propellant. This minimizes the likelihood of propellant tearing, cracking, and debonding. Tapers are also used to shape the thrust time curve and to soften thrust transients at tail-off. As a result, tapers are often used in high speed interceptor vehicles requiring thrust curve modifications. Tapers also minimize erosive burning effects and maximize volumetric loading fractions. This helps to increase the port-to-throat area ratio. The problem is that some ballistic codes do not account for the small tapered angles currently found in modern SRMs. This point was first raised by Clayton[10] in his original investigation of this generally overlooked feature of SRM analysis.

The issue here is that when ballistic codes refer to Culick's[1] or Taylor's[11] profiles to evaluate tapered chambers, the pressure drop can be overpredicted by as much as 25% to 80%. This is due to the velocity diminution that accompanies cross-sectional area increases. The reason: with an increase in flow area (decrease in velocity), the dynamic pressure depreciates, leading to an overall decrease in total pressure drop. In an effort to produce a solution that yields the proper pressure correction applicable to tapered combustion chambers, Clayton was able to obtain an approximate solution by employing a regular perturbation method.[10] Being asymptotic, Clayton's solution was shown to be reducible, at leading order, to Culick's profile for a taper angle of zero.

In 1956, Taylor[11] derived the solution for a rectangular chamber with porous walls as part of his treatment of injection-driven flows in channels, wedges, and cones. Other pertinent solutions were later advanced by Yuan and Finkelstein[12,13] and Terrill[14] who incorporated the effects of viscosity in both axisymmetric and planar domains. Their work was recently extended to include the effects of wall regression by Majdalani, Vyas, and Flandro,[15] and Zhou and Majdalani.[16]

The physical model to be employed here consists of the

[a)]Telephone: (931) 393-7280. Electronic mail: maji@utsi.edu

straight section of the motor followed by a tapered segment. The incorporation of the taper in the context of internal flowfield studies of SRMs seems to have received very little attention. In fact, one may find very few studies concerned with tapered chambers. One such study may be attributed to the work of Mu-Kuan and Tong-Miin.[17] In their attempt to understand the flowfield present in tapered ducts, Mu-Kuan and Tong-Miin conducted a fiber optic study of a nonuniform, injection-induced flow. The principal focus of their study was to determine the effect of the divergent configuration on the promotion of flow stability. Their study also confirmed the lack of similarity between the velocity distributions in straight (nontapered) and tapered chambers. It can hence be seen that the problem concerning SRMs with tapered walls will serve more than one purpose; particularly, it will help to elucidate the contrasting mean velocity distributions and compare the pressure drop between the parallel and tapered motor shapes. It will also address the mathematical peculiarities associated with the no-slip condition along the tapered surface. Finally, it will provide a more accurate baseline model for studying hydrodynamic instability of tapered grains such as those of Ariane and the Shuttle Reusable Solid Rocket Motor.

In searching for a solution that captures the effects of tapered walls, our methodology will exploit the vorticity at the surface and its transport along the streamlines. A relationship with the pressure gradient will permit the proper form of chamber vorticity to be ascertained. The development of an expression for the vorticity particular to tapered geometry will lead to a nonlinear governing differential equation for which a solution may be obtained by the method of regular perturbations.

Besides the perturbation solution, a numerical simulation will be performed and discussed. This will be accompanied by an error analysis to establish the physical limitations and bracket the applicability range of the resulting expressions.

II. MATHEMATICAL MODEL

The idealized tapered slab burner is characterized as a rectangular, porous duct with the top and bottom surfaces oriented at an angle α. The model is outlined in Fig. 1. This allows one to account for the bulk flow originating from the nontapered section of the motor. Accordingly, the origin for the coordinate system is expediently placed at the interface where $\bar{x}$ and $\bar{y}$ denote the axial and transverse coordinates, respectively. The nontapered section of the motor has dimensions of length L_0, height $2h_0$, and width w_0. The gases are injected across the top and bottom surfaces in a normal and uniform manner. As a consequence of mass conservation, the injected gases are forced to turn and assimilate with the primary bulk flow emanating from the straight section of the motor [see Fig. 1(a)].

A. Governing equations

Conceptualizing the problem at hand, it is instructive to note that the vorticity produced at the surface is an outgrowth of the interaction between the injected fluid and the axial pressure gradient. This phenomenon allows one to utilize an alternate form of Euler's momentum equation and the explicit relationship between chamber pressure and vorticity. Another feature of this governing set is that the vorticity is expressed in terms of the streamfunction. For the planar, two-dimensional model, the flow can be characterized as (i) steady, (ii) inviscid, (iii) incompressible, (iv) rotational, and (v) nonreactive. In accordance with the stated assumptions, the kinematic equations of motion can be written as

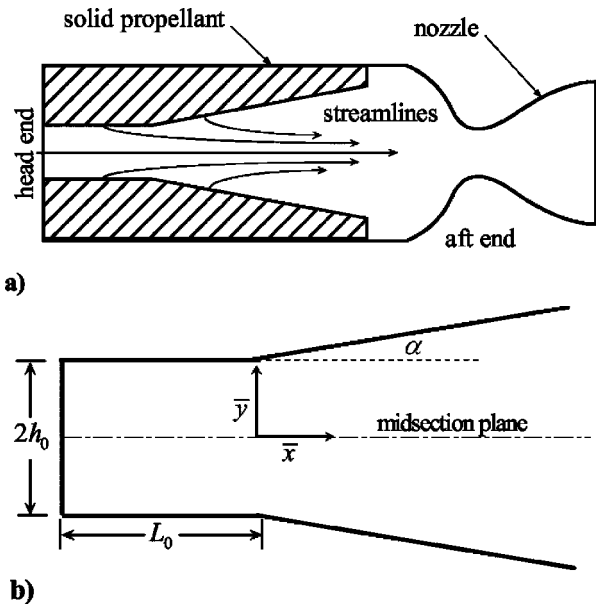

FIG. 1. Schematic featuring (a) typical slab burner configuration with tapered walls and (b) coordinate system used for the mathematical model.

$$\bar{\boldsymbol{u}} \cdot \bar{\nabla}\bar{\boldsymbol{u}} = -\bar{\nabla}\bar{p}/\rho, \tag{1}$$

$$\bar{\nabla}^2\bar{\psi} + \bar{\Omega}_z = 0, \tag{2}$$

and thus

$$\bar{u}_x\frac{\partial\bar{u}_x}{\partial\bar{x}} + \bar{u}_y\frac{\partial\bar{u}_x}{\partial\bar{y}} = -\frac{1}{\rho}\frac{\partial\bar{p}}{\partial\bar{x}}, \tag{3}$$

$$\bar{u}_x\frac{\partial\bar{u}_y}{\partial\bar{x}} + \bar{u}_y\frac{\partial\bar{u}_y}{\partial\bar{y}} = -\frac{1}{\rho}\frac{\partial\bar{p}}{\partial\bar{y}}, \tag{4}$$

$$\frac{\partial^2\bar{\psi}}{\partial\bar{x}^2} + \frac{\partial^2\bar{\psi}}{\partial\bar{y}^2} + \bar{\Omega}_z = 0, \tag{5}$$

where the overbar denotes dimensional variables.

B. Boundary conditions

Judicious boundary conditions are needed to obtain a closed-form solution that is representative of the physical model. To begin, one must recognize that the transverse component of velocity cannot physically contribute to the axial flow crossing into the tapered region at $\bar{x}=0$ (see Fig. 2). The needed boundary conditions are prescribed as follows: (i) inflow across the tapered interface must originate from the outflow of the nontapered segment of the motor; (ii) no flow

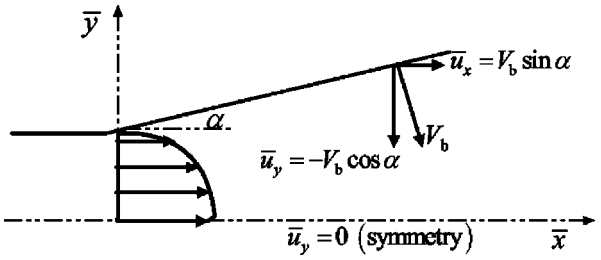

FIG. 2. Graphical depiction of the tapered segment with corresponding boundary conditions.

across the midsection plane; and (iii) uniform and constant, normal injection at the burning surface. Mathematically, these conditions are expressed as

$$\begin{aligned} &\bar{x}=0, \quad \forall\, \bar{y}, \quad \bar{u}_x = \tfrac{1}{2}\pi V_b (L_0/h_0)\cos\left(\tfrac{1}{2}\pi \bar{y}/h_0\right), \\ &\bar{y}=\bar{y}_s, \quad \forall\, \bar{x}, \quad \bar{u}_x = V_b \sin\alpha, \\ &\bar{y}=\bar{y}_s, \quad \forall\, \bar{x}, \quad \bar{u}_y = -V_b \cos\alpha, \\ &\bar{y}=0, \quad \forall\, \bar{x}, \quad \bar{u}_y = 0, \end{aligned} \tag{6}$$

where $\bar{y}_s$ is the ordinate of the tapered surface and V_b is the injection velocity at the propellant surface.

C. Normalization

Here, we use

$$x=\frac{\bar{x}}{h_0}; \quad y=\frac{\bar{y}}{h_0}; \quad L=\frac{L_0}{h_0}; \quad \nabla = h_0 \bar{\nabla}, \tag{7}$$

$$u_x=\frac{\bar{u}_x}{V_b}; \quad u_y=\frac{\bar{u}_y}{V_b}; \quad p=\frac{\bar{p}}{\rho V_b^2}, \tag{8}$$

$$\psi=\frac{\bar{\psi}}{h_0 V_b}; \quad \Omega=\frac{h_0 \bar{\Omega}}{V_b}. \tag{9}$$

Along with the nondimensional variables, the normalization of the boundary conditions yields

$$\begin{aligned} &x=0, \quad \forall\, y, \quad u_x = \tfrac{1}{2}\pi L \cos\left(\tfrac{1}{2}\pi y\right), \\ &y=y_s, \quad \forall\, x, \quad u_x = \sin\alpha, \\ &y=y_s, \quad \forall\, x, \quad u_y = -\cos\alpha, \\ &y=0, \quad \forall\, x, \quad u_y = 0. \end{aligned} \tag{10}$$

D. Mean velocity

The tapered slab geometry is based on the Cartesian coordinate system [as depicted in Fig. 1(b)] where $\bar{x}$ is the dimensional axial coordinate and $\bar{y}$ is the dimensional transverse coordinate. If the channel depth is w_0, then the area of the tapered burning surface, at any $\bar{x}$, will be given by

$$A_b = w_0 \bar{x} \sec\alpha. \tag{11}$$

Similarly, the chamber cross-sectional area may be evaluated from

$$A(\bar{x}) = w_0 (h_0 + \bar{x}\tan\alpha). \tag{12}$$

The inflow cross-sectional area at the interface of the tapered and straight portions of the chamber is simply $A_0 = w_0 h_0$. The corresponding bulk mean velocity becomes

$$\bar{u}_0 = (L_0/h_0) V_b. \tag{13}$$

Here, L_0 can be defined as the bulk flow parameter because it is directly proportional to the mean velocity at the entrance to the tapered portion. Due to mass conservation, the cross-sectional mean velocity of the fluid at any axial location $\bar{x}$ may be expressed by

$$\bar{u}_m(\bar{x}) = \frac{A_0 \bar{u}_0 + A_b V_b}{A(\bar{x})} = \frac{L_0 + \bar{x}\sec\alpha}{h_0 + \bar{x}\tan\alpha} V_b. \tag{14}$$

Expressing the resulting relation in normalized variables, one gets

$$u_m(x) = \frac{L + x\sec\alpha}{1 + x\tan\alpha}. \tag{15}$$

For the case of $\alpha = 0$, Eq. (15) reduces to

$$u_m = L + x. \tag{16}$$

which depicts the bulk flow in a straight duct with uniform injection.

To gain an in-depth understanding of the behavior of the bulk flow in tapered chambers at lengths sufficiently removed from the interface, Eq. (15) may be used to investigate the asymptotic behavior of the mean velocity. By so doing, one obtains

$$u_m(x) = (Lx^{-1} + \sec\alpha)(x^{-1} + \tan\alpha)^{-1}. \tag{17}$$

Evaluating the limit at $x \to \infty$ gives

$$\lim_{x\to\infty} u_m(x) = \csc\alpha. \tag{18}$$

As seen in Eq. (18), the mean velocity in a tapered chamber converges to a constant value as the axial distance approaches infinity (except for $\alpha = 0$). The result is due to mass conservation. The presence of the taper increases the flow area, thus attenuating the acceleration of the gases. In consequence, the velocity converges to a constant value, whereas the gases in a parallel chamber continue to accelerate at a constant rate. This behavior is illustrated in Fig. 3. The fact that the bulk flow velocity converges to a constant value suggests that the geometry imposes a restriction on the flow behavior in a combined motor configuration (Fig. 1). One may argue that the mean velocity in a tapered chamber must converge to a constant value. To suggest otherwise would constitute a violation of continuity. Hence, the mean velocity must be less than or equal to the maximum velocity that can be attained in a tapered motor. Mathematically, this can be expressed by

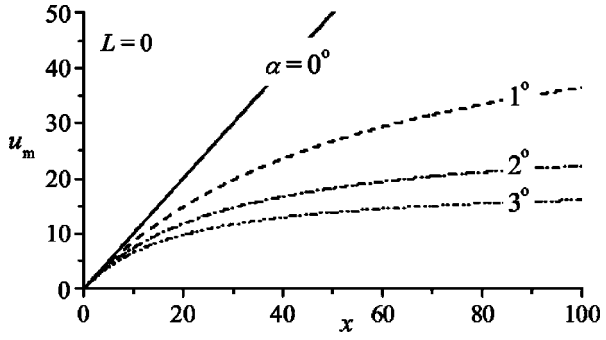

FIG. 3. Plot of average velocity down the channel as a function of taper angle.

$$u_{\mathrm{m}}(x)\big|_{\alpha=0^{\circ}} \leqslant u_{\mathrm{ave}}(\infty) \quad \text{or} \quad L+x \leqslant \csc\,\alpha. \tag{19}$$

Rearranging and expressing the result from Eq. (19) in dimensional variables, one obtains

$$\alpha(L_0+\bar{x}) \leqslant h_0, \tag{20}$$

where $\sin\,\alpha \approx \alpha$ for small values of α. The selection of geometric motor parameters that satisfy Eq. (20) ensures that the solution observes continuity.

E. Streamfunction along the burning surface

A crucial component to the formulation of the flowfield under study is the development of the streamfunction at the simulated burning surface. The nature of the streamfunction changes with the angular orientation of the burning surface. Therefore, one can define the directional derivative along the burning surface as

$$\frac{\mathrm{d}\psi_{\mathrm{s}}}{\mathrm{d}s} = \frac{\partial\psi_{\mathrm{s}}}{\partial x}\frac{\mathrm{d}x}{\mathrm{d}s} + \frac{\partial\psi_{\mathrm{s}}}{\partial y}\frac{\mathrm{d}y}{\mathrm{d}s} = \frac{\partial\psi_{\mathrm{s}}}{\partial x}\cos\,\alpha + \frac{\partial\psi_{\mathrm{s}}}{\partial y}\sin\,\alpha. \tag{21}$$

Along the burning surface (see Fig. 4), the normalized variables are evaluated to be

$$x = s\,\cos\,\alpha, \tag{22}$$

$$y_{\mathrm{s}} = 1 + s\,\sin\,\alpha = 1 + x\,\tan\,\alpha, \tag{23}$$

$$u_{x,\mathrm{s}} = \sin\,\alpha, \tag{24}$$

$$u_{y,\mathrm{s}} = -\cos\,\alpha. \tag{25}$$

Making use of the streamfunction relations as defined at the burning surface, one sets

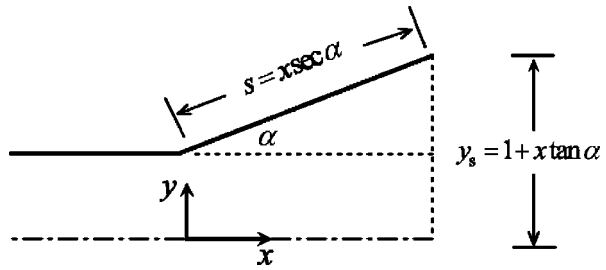

FIG. 4. Schematic of tapered segment showing key geometric parameters in dimensionless form.

$$u_{x,\mathrm{s}} = \frac{\partial\psi_{\mathrm{s}}}{\partial y}, \quad u_{y,\mathrm{s}} = -\frac{\partial\psi_{\mathrm{s}}}{\partial x}. \tag{26}$$

Subsequent insertion of the streamfunction definitions into Eq. (21) yields

$$\frac{\mathrm{d}\psi_{\mathrm{s}}}{\mathrm{d}s} = \cos^2\,\alpha + \sin^2\,\alpha = 1. \tag{27}$$

Integrating the resulting expression and converting back to the spatial coordinates, one obtains $\psi_{\mathrm{s}}(s)=s+C$ or

$$\psi_{\mathrm{s}}(x) = x\,\sec\,\alpha + C, \tag{28}$$

where C is a constant that can be evaluated by applying the boundary condition, $\psi_{\mathrm{s}}(0)=L$. Application of this constraint gives

$$\psi_{\mathrm{s}}(x) = x\,\sec\,\alpha + L. \tag{29}$$

Note that the mean velocity can be expressed as

$$u_{\mathrm{m}}(x) = \frac{\psi_{\mathrm{s}}}{y_{\mathrm{s}}}. \tag{30}$$

This relation will be used to simplify the forthcoming analysis.

F. Axial pressure gradient

Essential to the development of the chamber vorticity is the derivation of the axial pressure gradient. To begin, one may start by expressing Bernoulli's equation along the central streamline as

$$p(x) = p_0 - \tfrac{1}{2}u_{\mathrm{max}}^2(x). \tag{31}$$

The total pressure in the combustion chamber of SRMs is sensitive to the shape of the axial profiles. In nontapered chambers, the shape of the axial profile is determined by the ratio of the axial velocity to the axial distance. For diverging ducts, the axial profile changes at the burning surface as the gases move downstream. Thus, it is required that the shape of the profile be known at each axial location in order to obtain accurate pressure estimates. Considering that the maximum velocity is unknown, it is expedient to define a ratio between the maximum and mean local velocities at any axial location x. This velocity ratio can be written as

$$\beta(x) = \frac{u_{\mathrm{max}}(x)}{u_{\mathrm{m}}(x)}. \tag{32}$$

The form of $\beta(x)$ will be later determined to satisfy the no-slip condition along the tapered burning surface. By substituting Eq. (32) into Eq. (31), the expression for the pressure becomes

$$p(x) = p_0 - \tfrac{1}{2}\beta^2(x)u_{\mathrm{m}}^2(x). \tag{33}$$

The pressure gradient can be determined along the surface by calculating the derivative of Eq. (33). The result is

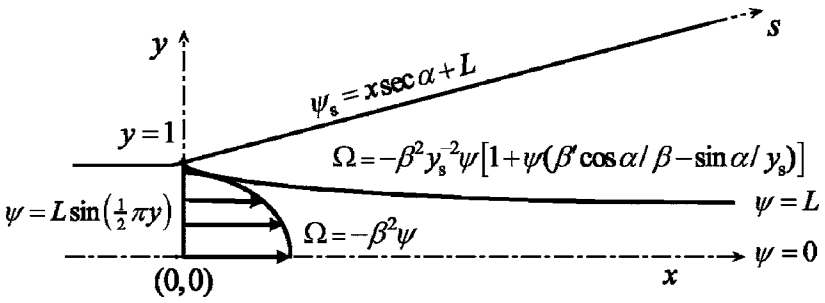

FIG. 5. Evaluation of the streamfunction along the boundaries. Also shown is the key relation linking vorticity at any point along a streamline to the streamfunction at the surface; the latter remains constant along any streamline crossing the chamber length.

$$\frac{\partial p}{\partial x} = -\beta^2(x)u_{\mathrm{m}}(x)\left[\frac{\mathrm{d}u_{\mathrm{m}}(x)}{\mathrm{d}x} + \frac{u_{\mathrm{m}}(x)}{\beta(x)}\frac{\mathrm{d}\beta(x)}{\mathrm{d}x}\right]. \tag{34}$$

Differentiating Eq. (15) and substituting the known surface variables furnishes, in turn,

$$\frac{\mathrm{d}u_{\mathrm{m}}}{\mathrm{d}x} = \frac{\sec\alpha}{y_{\mathrm{s}}} - \frac{\psi_{\mathrm{s}}\tan\alpha}{y_{\mathrm{s}}^2}. \tag{35}$$

By substituting Eq. (35) into Eq. (34) and simplifying, it follows that

$$\frac{\partial p}{\partial x} = -\frac{\beta^2\psi_{\mathrm{s}}\sec\alpha}{y_{\mathrm{s}}^2}\left[1 - \frac{\psi_{\mathrm{s}}\sin\alpha}{y_{\mathrm{s}}} + \psi_{\mathrm{s}}\cos\alpha\left(\frac{\beta'}{\beta}\right)\right], \tag{36}$$

where

$$\beta' = \frac{\mathrm{d}\beta}{\mathrm{d}x}. \tag{37}$$

G. Surface vorticity

The relationship between the chamber streamfunction and pressure is now established. Next, one may seek evaluation of the momentum equation for steady, inviscid flows at the surface. Recalling the normalized form of Euler's momentum equation for steady, incompressible, and inviscid flows,

$$\boldsymbol{u}\cdot\nabla\boldsymbol{u} = -\nabla p, \tag{38}$$

one may substitute the well known vector identity, $\boldsymbol{u}\cdot\nabla\boldsymbol{u} = \nabla(\frac{1}{2}\boldsymbol{u}\cdot\boldsymbol{u}) - \boldsymbol{u}\times(\nabla\times\boldsymbol{u})$, to obtain an alternate expression of the form

$$\boldsymbol{u}\times\boldsymbol{\Omega} = \nabla\left(p + \tfrac{1}{2}\boldsymbol{u}\cdot\boldsymbol{u}\right). \tag{39}$$

The velocity vector at the simulated burning surface is defined as

$$\boldsymbol{u}_{\mathrm{s}} = \sin\alpha\hat{\mathbf{i}} - \cos\alpha\hat{\mathbf{j}}. \tag{40}$$

Evaluating the left-hand side of Eq. (39) gives, at the surface,

$$\begin{aligned}\boldsymbol{u}_{\mathrm{s}}\times\boldsymbol{\Omega}_{\mathrm{s}} &= (\sin\alpha\hat{\mathbf{i}} - \cos\alpha\hat{\mathbf{j}})\times(\Omega_{\mathrm{s}}\hat{\mathbf{k}}) \\ &= -\Omega_{\mathrm{s}}(\cos\alpha\hat{\mathbf{i}} + \sin\alpha\hat{\mathbf{j}}) = -\Omega_{\mathrm{s}}\hat{\mathbf{s}},\end{aligned} \tag{41}$$

where $\hat{\mathbf{s}}$ represents the unit vector parallel to the burning surface. As with the directional derivative of the streamfunction, the chain rule can be applied to the pressure gradient along the surface. Thus, we write

$$\frac{\mathrm{d}p}{\mathrm{d}s}\hat{\boldsymbol{s}} = \left(\frac{\partial p}{\partial x}\frac{\mathrm{d}x}{\mathrm{d}s} + \frac{\partial p}{\partial y}\frac{\mathrm{d}y}{\mathrm{d}s}\right)\hat{\boldsymbol{s}} = \left(\frac{\partial p}{\partial x}\cos\alpha + \frac{\partial p}{\partial y}\sin\alpha\right)\hat{\boldsymbol{s}}. \tag{42}$$

Equating the expressions provided by Eqs. (41) and (42) yields

$$\Omega_{\mathrm{s}} = -\frac{\partial p}{\partial x}\cos\alpha - \frac{\partial p}{\partial y}\sin\alpha. \tag{43}$$

Considering values of α between 1° and 3°, any term containing $\sin\alpha$ would appear to be negligible. Taking this into account, Eq. (43) can be reduced to

$$\Omega_{\mathrm{s}} = -\frac{\partial p}{\partial x}\cos\alpha + O(\alpha V_{\mathrm{b}}^2). \tag{44}$$

Having previously formulated a relation for the pressure gradient in Eq. (36), the surface vorticity can be expressed as

$$\Omega_{\mathrm{s}} = \frac{\beta^2\psi_{\mathrm{s}}}{y_{\mathrm{s}}^2}\left[1 - \frac{\psi_{\mathrm{s}}\sin\alpha}{y_{\mathrm{s}}} + \psi_{\mathrm{s}}\cos\alpha\left(\frac{\beta'}{\beta}\right)\right]. \tag{45}$$

Figure 5 allows one to visually interpret the pertinent surface and chamber quantities that are essential to formulate the governing equation for mean flow in tapered ducts. Shown in the diagram are the domains for which the required form of the vorticity is given. Also shown are the values of the streamfunction at the boundaries, which will be used later to obtain a closed-form solution.

III. REGULAR PERTURBATIONS

At this point, one may recall that vorticity is produced at the surface from the interaction between the perpendicularly injected gases and the axial pressure gradient. The primary feature particular to the vortical behavior of an inviscid fluid is the fact that the vorticity generated at the surface is conserved along the streamlines as the gases penetrate into the chamber. This suggests that the expression for the surface vorticity is now valid (along the streamlines) throughout the chamber. Therefore, one may drop the subscript from the streamfunction and vorticity variables in Eq. (45). Next, one may equate Eq. (5) with Eq. (45) to obtain a partial, nonlinear differential equation that governs the flow. Equating these expressions, one gets

$$\frac{\partial^2\psi}{\partial x^2}+\frac{\partial^2\psi}{\partial y^2}=-\frac{\beta^2\psi}{y_s^2}\left[1-\frac{\psi\sin\alpha}{y_s}+\psi\cos\alpha\left(\frac{\beta'}{\beta}\right)\right]. \quad (46)$$

The boundary conditions required to solve Eq. (46) are given by

$$\psi(x,0)=0; \quad \psi(x,y_s)=\psi_s;$$
$$\frac{\partial\psi(0,y)}{\partial y}=\frac{1}{2}\pi L\cos\left(\frac{1}{2}\pi y\right); \quad \frac{\partial\psi(x,0)}{\partial x}=0. \quad (47)$$

For the cylindrical case, Clayton[10] determined the relative magnitudes of the axial derivatives of the streamfunction and the velocity ratio by numerical analysis. His results enabled him to deduce that the axial derivatives were negligibly small. In particular, Clayton noted that β' and $\partial^2\psi/\partial x^2$ were small quantities. These observations may be verified using a scaling analysis. Considering that

$$\frac{\partial^2\psi}{\partial x^2}=\frac{\partial u_y}{\partial x}, \quad (48)$$

one may recall that the transverse velocity is independent of x in the straight channel (thus causing $\partial^2\psi/\partial x^2$ to vanish). Evidently, the presence of a small taper will not affect the size of this term. We can safely assume that the axial derivatives are so small that they can be neglected in the tapered domain. Using arguments similar to those provided by Clayton, one can reduce Eq. (46) into

$$\frac{\partial^2\psi}{\partial y^2}=-\frac{\beta^2\psi}{y_s^2}\left(1-\frac{\psi\sin\alpha}{y_s}\right). \quad (49)$$

Recognizing that the reduced equation is nonlinear, a solution can be sought by the method of regular perturbations. Accordingly, the streamfunction and velocities may be expanded in the form

$$\psi=\psi_0+\varepsilon\psi_1+O(\varepsilon^2), \quad (50)$$

$$\mathbf{u}=\mathbf{u}_0+\varepsilon\mathbf{u}_1+O(\varepsilon^2). \quad (51)$$

Similarly, in an effort to assure satisfaction of the no-slip condition along the tapered surface, one can write

$$\beta=\beta_0+\varepsilon\beta_1+O(\varepsilon^2), \quad (52)$$

where the perturbation parameter is due to the small taper angle; namely,

$$\varepsilon=\sin\alpha. \quad (53)$$

The governing equation can be solved by first inserting Eqs. (50) and (52) into Eq. (49) and expanding the resulting terms. This effort serves to linearize the governing equation by reducing it to a sequence of linear problems.

A. Leading-order solution

For the sake of brevity, the details of the expansion are not presented here. At leading order, $O(1)$, one obtains

$$\frac{\partial^2\psi_0}{\partial y^2}+\frac{\beta_0^2\psi_0}{y_s^2}=0. \quad (54)$$

The general solution can be expressed as

$$\psi_0=C_1\cos\left(\beta_0\frac{y}{y_s}\right)+C_2\sin\left(\beta_0\frac{y}{y_s}\right). \quad (55)$$

Now that a general solution has been obtained, evaluation of Eq. (55) at the conditions provided by Eq. (47) furnishes the leading-order solution

$$\psi_0=\psi_s\sin\left(\beta_0\frac{y}{y_s}\right), \quad (56)$$

where, from Eq. (29), $\psi_s=x\sec\alpha+L$, and

$$\beta_0=\tfrac{1}{2}\pi. \quad (57)$$

It should be noted that at $L=\alpha=0$, one recovers

$$\psi_0=x\sin(\beta_0 y). \quad (58)$$

Equation (58) represents Taylor's profile for porous channel flow.[11] The leading-order solution, given by Eq. (56), can be described as an expanded version of the Taylor profile. Such a form can be attributed to the bulk flow variation resulting from the increased surface area that is precipitated by the divergent angle.

B. First-order solution

At first order, the perturbative expansion yields

$$\frac{\partial^2\psi_1}{\partial y^2}+\frac{\beta_0^2\psi_1}{y_s^2}+\frac{2\beta_0\beta_1\psi_0}{y_s^2}-\frac{\beta_0^2\psi_0^2}{y_s^3}=0. \quad (59)$$

The first-order boundary conditions are

$$\psi_1(x,0)=0; \quad \psi_1(x,y_s)=0. \quad (60)$$

By application of these boundary conditions, one obtains a first-order correction of the form

$$\psi_1(x,y)=\frac{\psi_s}{6y_s}\left[3\psi_s+\psi_s\cos\left(2\frac{\beta_0 y}{y_s}\right)-2\psi_s\sin\left(\frac{\beta_0 y}{y_s}\right)-4\psi_s\cos\left(\frac{\beta_0 y}{y_s}\right)+6y\beta_1\cos\left(\frac{\beta_0 y}{y_s}\right)\right]. \quad (61)$$

The first-order correction accounts for transverse expansion, flow deceleration, and the axial derivatives. Observing Eq. (61), it can be seen that there exists an unknown term that originates from the perturbed velocity ratio β. The final step in the solution process involves solving for the first-order velocity ratio β_1, such that the no-slip condition is satisfied along the tapered surface. In the process, it is necessary to express the surface velocity using

$$u_s=u_x\cos(\alpha)+u_y\sin(\alpha)=u_{s,0}+\varepsilon u_{s,1}, \quad (62)$$

and thus

$$u_s = \frac{\partial \psi}{\partial y}\cos(\alpha) - \frac{\partial \psi}{\partial x}\sin(\alpha)$$
$$= (\psi_0 + \varepsilon\psi_1)_y \cos(\alpha) - (\psi_0 + \varepsilon\psi_1)_x \sin(\alpha). \quad (63)$$

Considering that ψ_0 already satisfies the no-slip condition at the wall, one may segregate the first-order correction by writing

$$u_{s,1} = \frac{\partial \psi_1}{\partial y}\cos(\alpha) - \frac{\partial \psi_1}{\partial x}\sin(\alpha). \quad (64)$$

Again, it can be seen that the term containing $\sin(\alpha)$ is $O(\varepsilon)$. One may ignore this term and set Eq. (64) equal to zero. Evaluating the resulting expression at the tapered surface gives

$$\beta_1 = \frac{2}{3}\frac{\psi_s}{y_s} = \frac{2}{3}u_m. \quad (65)$$

The required forms of the leading- and first-order velocity ratios, β_0 and β_1, respectively, are thus determined.

IV. VELOCITY, PRESSURE, AND VORTICITY

Now that the proper form of the streamfunction has been ascertained, it is possible to extract other useful physical quantities particular to tapered flowfields. A useful analysis of the remaining flow attributes can be made from both the leading-order and first-order solutions. The incorporation of the first-order correction ensures that the physical characteristics consistent with flow in tapered geometries are recovered at larger taper angles and axial distances. In particular, the addition of higher-order corrections may be deemed necessary for the axial velocity and the pressure drop, ensuring a reasonably accurate solution suitable for comparison with its numerical counterpart. Although the distance to the tapered surface is a function of the axial coordinate x, it may be treated as a constant in the evaluation of the velocity, pressure, and vorticity. This enables one to express the desired quantities in a compact and concise form similar to the leading-order solution. Forthwith, one can compute the velocity components from the definition of the streamfunction. For simplicity, we define

$$\eta = \beta_0 \frac{y}{y_s}. \quad (66)$$

The expressions for the leading- and first-order streamfunctions become

$$\psi_0(x,y) = \psi_s \sin\,\eta \quad (67)$$

and

$$\psi_1(x,y) = \frac{\psi_s}{6y_s}[3\psi_s + \psi_s\cos(2\eta) - 2\psi_s \sin\,\eta - 4\psi_s \cos\,\eta + 6y\beta_1 \cos\,\eta]. \quad (68)$$

The leading-order axial velocity component reduces to

$$u_{x,0} = \frac{\partial \psi_0}{\partial y} = \frac{\beta_0 \psi_s}{y_s}\cos\,\eta = \beta_0 u_m \cos\,\eta. \quad (69)$$

The first-order correction for the axial velocity component follows; specifically,

$$u_{x,1} = \frac{\partial \psi_1}{\partial y} = \frac{\psi_s}{3y_s^2}[(3\beta_1 y_s - \beta_0\psi_s)\cos\,\eta + \beta_0(2\psi_s - 3\beta_1 y)\sin\,\eta - \beta_0\psi_s \sin(2\eta)], \quad (70)$$

which can be conveniently written in terms of the mean velocity as

$$u_{x,1} = \tfrac{1}{3}u_m^2[(2-\beta_0)\cos\,\eta + 2(\beta_0 - \eta)\sin\,\eta - \beta_0 \sin(2\eta)]. \quad (71)$$

Subsequently, the total solution for the axial velocity can be concisely expressed as

$$u_x = u_{x,0} + \varepsilon u_{x,1}. \quad (72)$$

In like manner, the leading-order solution for the transverse velocity component is found to be

$$u_{y,0} = -\frac{\partial \psi_0}{\partial x} = -\sec(\alpha)\sin\,\eta. \quad (73)$$

The first-order transverse velocity component, which is written as

$$u_{y,1} = -\frac{\partial \psi_1}{\partial x} = -\frac{\partial \psi_1}{\partial \psi_s}\frac{d\psi_s}{dx} - \frac{\partial \psi_1}{\partial y_s}\frac{dy_s}{dx}$$
$$= -\frac{\partial \psi_1}{\partial \psi_s}\frac{d\psi_s}{dx} - \tan\,\alpha\frac{\partial \psi_1}{\partial y_s} = -\frac{\partial \psi_1}{\partial \psi_s}\frac{d\psi_s}{dx} + O(\varepsilon). \quad (74)$$

At first order, the $O(\varepsilon)$ terms in $u_{y,1}$ become $O(\varepsilon^2)$; we only need to evaluate the first term in Eq. (74); namely,

$$u_{y,1} = -\frac{\psi_s \sec\,\alpha}{3y_s}\left[3 + \cos(2\eta) - 2\sin\,\eta - 4\cos\,\eta + 4\frac{y}{y_s}\cos\,\eta\right] + O(\varepsilon). \quad (75)$$

Equation (75) can be further simplified to give

$$u_{y,1} = -\tfrac{1}{3}u_m \sec\,\alpha\,[3 + \cos(2\eta) - 2\sin\,\eta - 4\cos\,\eta + (8/\pi)\eta\cos\,\eta] + O(\varepsilon). \quad (76)$$

So far, it has been established that the parameter of interest is the pressure drop. The latter is extremely sensitive to the axial velocity profile (which is governed by the height of the chamber). Quite naturally, approximating the chamber height as a constant in the axial direction introduces error. This error can be alleviated by the addition of the first-order correction.

Having formulated the velocity field, the pressure gradients can be deduced straightforwardly. In order to obtain the required pressure drop along the chamber length, one only needs to insert the axial and transverse velocity relations into the inviscid momentum equations given by Eqs. (3) and (4). By performing this substitution, one gets

$$\frac{\partial p_0}{\partial x} = -\frac{\beta_0^2 \psi_s \sec\alpha}{y_s^2}, \tag{77}$$

$$\frac{\partial p_0}{\partial y} = -\frac{\beta_0 \sec^2\alpha}{2y_s} \sin\left(\frac{2\beta_0 y}{y_s}\right). \tag{78}$$

By integrating and combining Eqs. (77) and (78), one is able to produce the spatial variation of the pressure that satisfies both momentum equations. Consequently, the total pressure at leading order can be expressed as

$$p_{t,0}(x,y) = -\frac{\beta_0^2}{2y_s^2} x \sec\alpha (x\sec\alpha + 2L) + \frac{1}{4}\cos\left(2\beta_0 \frac{y}{y_s}\right)\sec^2\alpha + C_0. \tag{79}$$

The head-end boundary condition is $p(0,0)=p_{\text{Taylor}}$, where $p_{\text{Taylor}}=-\frac{1}{2}\beta_0^2 L^2$. By applying this condition, the constant becomes $C_0=\frac{1}{2}\beta_0^2 L^2-\frac{1}{4}\sec^2\alpha$. Setting $\Delta p_{t,0}=p_{t,0}(x,y)-p_{\text{Taylor}}$, one can express the leading-order pressure drop along $y=0$ in the following compact form:

$$\Delta p_{t,0} = -\frac{\beta_0^2 x \sec\alpha}{2y_s^2}(x\sec\alpha + 2L). \tag{80}$$

We note that the treatment of y_s as a constant has permitted the development of an approximate expression for the pressure drop at leading order. Thus, it may be reasonable to question the accuracy of the derivation due to the attendant approximations. To arrive at an expression for the pressure drop, y_s has been assumed to be constant twice for purposes of differentiation and once for integration, thereby compounding the errors involved. For larger taper angles, the variation of half-height with axial distance increases, thus leading to the possibility of underprediction of the pressure drop for larger values of α. In an effort to recover the accuracy of the model presented here, the pressure drop at first order is considered. The expression is obtained in the same manner as its leading-order solution for pressure with the addition of a term that is of first order. Thus, in the interest of conciseness, the details regarding the derivation are not presented here. The complete relation, including both the leading- and first-order terms, at $L=0$, can be expressed as

$$\begin{aligned}\Delta p(x;\varepsilon) &= -\frac{\beta_0^2 x^2 \sec^2\alpha}{2y_s^2} - \varepsilon\frac{x^2\sec^4\alpha}{72y_s^4} \times[x^2(6\pi^2-8\pi+8)-39y_s^2]+\cdots \\ &= -\frac{\pi^2 x^2\sec^2\alpha}{8y_s^2}\left\{1+\varepsilon\frac{\sec^2\alpha}{9\pi^2 y_s^2}[x^2(6\pi^2-8\pi+8) - 39y_s^2]+\cdots\right\}.\end{aligned} \tag{81}$$

It has been determined earlier that the pressure gradient in the transverse direction is negligibly small. This leaves the axial pressure gradient as the quantity of interest.

In addition to the formulation of the velocity and pressure gradients, one may compute the vorticity using

$$\Omega(x,y) = \frac{\beta_0^2\psi_s}{y_s^2}\sin\left(\beta_0\frac{y}{y_s}\right). \tag{82}$$

Each of the required flowfield characteristics particular to tapered slab burners is now at hand. Although some mathematical similarities *appear* to exist between flow in tapered and straight chambers, models for straight chambers do not encompass all of the physical characteristics inherent in the present model. Since the taper angle is known to be small, it follows that the leading-order mean flow characteristics possess minimal variance with the taper angle α. However, this is not the case given that the parameter that is most sensitive to the taper is the pressure field.

In order to explore the effects of placing a straight grain upstream of the tapered segment, one may invoke another parameter that arises from this study. This parameter has been described as the bulk flow parameter $L=u_0$; it is also known as the normalized chamber length $L=L_0/h_0$. The bulk flow parameter enables one to examine the physical characteristics of small to moderate sized motors with combined geometry.

Having completed the analytical treatment, the key components of the perturbation solution are presented in Table I alongside their counterparts arising in the axisymmetric flow analog with circular cross section.[18]

V. COMPUTATIONAL FLUID DYNAMICS VALIDATION

Thus far, we have explored the characteristics of mean flowfields applicable to the slab motor with available analytical procedures. En route to obtaining an analytical solution that encompasses the physical significance of mean flow in tapered and parallel SRM combustion chambers, the first- and second-order axial derivatives of the parameters essential to this work were assumed to be negligible. For the case of the tapered cylindrical motor originally formulated by Clayton, a numerical computation was performed in an effort to determine the relative magnitudes of these terms in the governing equations. Close examination of the terms revealed that they were indeed negligible and significant error would not accrue in their absence; hence, an analytical solution was possible by the method of regular perturbations. The same reasoning can be adopted for the mean flow model in a slab burner. Along similar lines, a numerical simulation can be employed to further assist in the verification and assessment of pertinent parameters critical to the applicability of these closed-form solutions. To that end, a numerical simulation is pursued. A widely used finite volume solver will be employed to simulate the mean flowfield characteristics of tapered chambers.

A. Geometry and meshing scheme

The geometric model for the Cartesian geometry is created for taper angles ranging from 1° to 3°. The dimensions are chosen in accordance with the parameters used by the analytical model. The slab is modeled in two-dimensional space with the simulated burning surfaces defined as velocity inlets.

TABLE I. Comparison between Cartesian and cylindrical solutions for the internal flowfield in a tapered chamber.

Planar solution: Tapered slab	Axisymmetric solution: Tapered cylinder
$\psi_s(x)=x\sec\alpha+L$	$\psi_s(z)=z\sec\alpha\left(1+\frac{1}{2}z\tan\alpha\right)+L$
$y_s=1+x\tan\alpha$	$r_s=1+z\tan\alpha$
$\Omega_s=\frac{\beta^2\psi_s}{y_s^2}\left[1-\frac{\psi_s\sin\alpha}{y_s}+\psi_s\cos\alpha\left(\frac{\beta'}{\beta}\right)\right]$	$\Omega_s=4\beta^2\frac{\psi_s}{r_s^3}\left[1-2\frac{\psi_s\sin\alpha}{r_s^2}+\frac{\psi_s\cos\alpha}{r_s}\left(\frac{\beta'}{\beta}\right)\right]$
$\Omega=\frac{\beta^2\psi}{y_s^2}\left[1-\frac{\psi\sin\alpha}{y_s}+\psi\cos\alpha\left(\frac{\beta'}{\beta}\right)\right]$	$\Omega=4\beta^2 r\frac{\psi}{r_s^4}\left[1-2\frac{\psi\sin\alpha}{r_s^2}+\frac{\psi\cos\alpha}{r_s}\left(\frac{\beta'}{\beta}\right)\right]$
$u_m=\frac{\psi_s}{y_s}=\frac{x\sec\alpha+L}{1+x\tan\alpha}$	$u_m=2\frac{\psi_s}{r_s^2}=2\frac{z\sec\alpha\left(1+\frac{1}{2}z\tan\alpha\right)+L}{(1+z\tan\alpha)^2}$
$\beta_0=\frac{1}{2}\pi$	
$\beta_1=\frac{2}{3}\frac{\psi_s}{y_s}=\frac{2}{3}u_m$	$\beta_1=\frac{4}{3}\frac{\psi_s}{r_s^2}=\frac{2}{3}u_m$
$\eta=\beta_0\frac{y}{y_s}=\frac{\pi y}{2(1+x\tan\alpha)}$	$\eta=\beta_0\frac{r^2}{r_s^2}=\frac{\pi r^2}{2(1+z\tan\alpha)^2}$
$\psi_0=\psi_s\sin\eta$	
$\psi_1=\frac{1}{6}u_m\psi_s[3+\cos(2\eta)-2\sin\eta-4\cos\eta+(8/\pi)\eta\cos\eta]$	
$u_{x,0}=u_{z,0}=\frac{1}{2}\pi u_m\cos\eta$	
$u_{x,1}=u_{z,1}=\frac{1}{3}u_m^2\left[\left(2-\frac{1}{2}\pi\right)\cos\eta+(\pi-2\eta)\sin\eta-\frac{1}{2}\pi\sin(2\eta)\right]$	
$u_{y,0}=-\sec\alpha\sin\eta$	$u_{r,0}=-\frac{r_s}{r}\sec\alpha\sin\eta=-\frac{(1+z\tan\alpha)}{r}\sec\alpha\sin\eta$
$u_{y,1}=-\frac{u_m}{3}\sec\alpha\left[\begin{matrix}3+\cos(2\eta)-2\sin\eta\\-4\cos\eta+(8/\pi)\eta\cos\eta\end{matrix}\right]$	$u_{r,1}=-\frac{u_m}{3}\sec\alpha\frac{(1+z\tan\alpha)}{r}\left[\begin{matrix}3+\cos(2\eta)-2\sin\eta\\-4\cos\eta+(8/\pi)\eta\cos\eta\end{matrix}\right]$
$\Delta p_{t,0}=-\frac{\pi^2 x\sec\alpha}{8(1+x\tan\alpha)^2}(x\sec\alpha+2L)$	$\Delta p_{t,0}=-\frac{\pi^2 z\sec\alpha}{2(1+z\tan\alpha)^4}(z\sec\alpha+2L)$

The meshing scheme and interval sizes are generally chosen based on the size and complexity of the physical model. Since the model under study possesses relatively simple geometry, standard meshing schemes are utilized to obtain a numerical solution with an interval size of 0.1.

B. Governing equations and numerical discretization

The governing equations are the steady-state incompressible Navier-Stokes equations with constant properties

$$\bar{\nabla}\cdot\bar{\boldsymbol{u}}=0,$$
$$\bar{\boldsymbol{u}}\cdot\bar{\nabla}\bar{\boldsymbol{u}}=\mu\bar{\nabla}^2\bar{\boldsymbol{u}}-\frac{1}{\rho}\bar{\nabla}\bar{p}. \tag{83}$$

The finite volume method is used to carry out the discretization of Eqs. (83). In short, the governing equations are integrated over each of the domain control volumes, yielding an algebraic equation that relates neighboring values of the dependent variable to those at the centroid of each control volume. In the process, specific interpolation methods are used to relate face values to control volume values, such as the upwind and QUICK schemes for the convection term. In our simulations, we have used second-order schemes for all terms, while the pressure velocity coupling is resolved using the SIMPLE algorithm.

C. Boundary and operating conditions

The working fluid is injected at velocities ranging from 0.1 to 1 m/s. This choice is based on the experimental work by Brown *et al.*[19,20] and Dunlap *et al.*[21,22] In addition, the selected range is corroborated by Clayton's computational fluid dynamics results; the latter suggest that the taper profiles change minimally with increasing injection velocity provided that the Reynolds numbers remain within the range of 10^2 to 10^4.[10] Concerning the reference pressure, it can be interpreted as a boundary condition for the stagnation pressure at the head end of the chamber and, as a result, is placed at the origin. This condition is chosen so that the mass outflow condition at the outlet of the chamber is not affected. It also allows the pressure to vanish at the head end.

The theoretical model chosen here for the numerical solution is valid for laminar incompressible fluids. The flowfield inside an actual SRM can be turbulent and a significant portion of the combustion occurs near the burning surface so that the chamber is filled primarily with the reaction products (see Chu, Yang, and Majdalani[23] and Vyas, Majdalani, and Yang[24]).

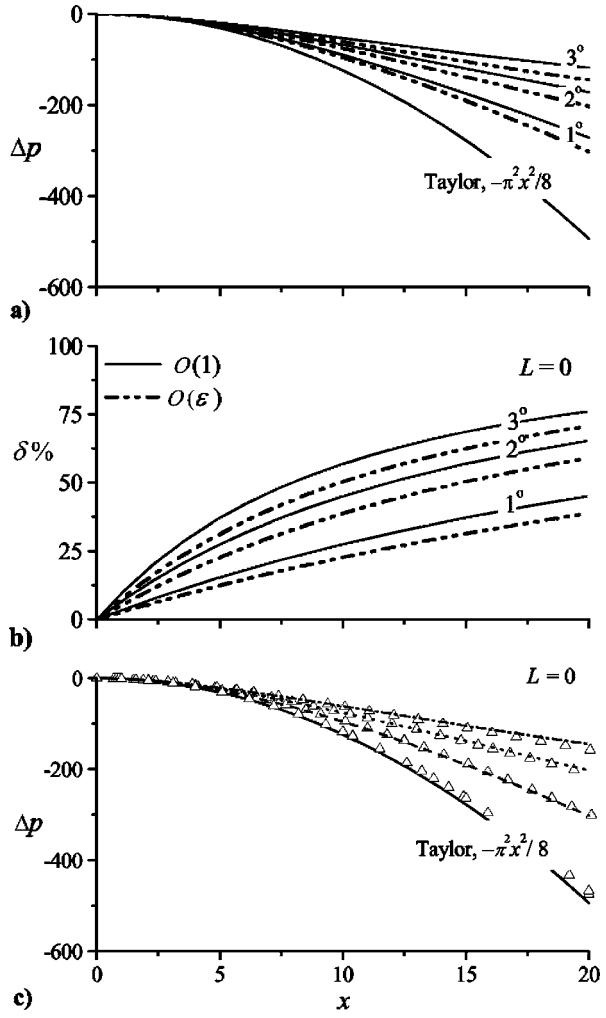

FIG. 6. We plot in (a) both leading- and first-order pressure drop approximations for several values of taper angle α. In (b) the percent overprediction from (a) is calculated and shown at several values of α. In (c) we compare numerical versus first-order solutions.

VI. RESULTS AND DISCUSSION

This section seeks to document and compare the dissimilarities that exist between the numerical and analytical solutions. With graphical depictions of the quantities in question, one is able to determine the level of accuracy that is required and which physical parameters are most important. For the case of tapered SRMs, it has been determined that the axial velocity profiles and the pressure drop are of paramount importance. To validate the underlying assumptions made so far, the same problem is solved numerically. Here, a comparison with computations is performed with the aim of elucidating the similarities, differences and limitations of the analytical solution. Also in question will be the magnitude of the axial derivatives. This portion of the final analysis will be critical given the assumption of constant distance from the midsection plane to the simulated burning surface.

A. Pressure approximations

As seen in Fig. 6(a), it is clear that the pressure varies with the taper angle. The slow increase in cross-sectional area acts to decrease the pressure drop by allowing a slight buildup in local static pressure (resulting from the accompanying decrease in velocity). As it can be inferred from Fig. 6(a), larger motors are seen to exhibit a higher sensitivity to small increases in wall taper. Even in chambers with zero bulk flow, one can infer that the influence of minute variations in wall taper can have significant impact on the overall pressure drop. By comparison to Taylor's solution in a straight porous channel, Fig. 6(a) illustrates the sharp decreases in the absolute pressure drop at higher taper angles taken along the midsection plane ($y=0$). In a tapered motor for which the actual pressure drop down the bore is 100 psi, modeling without account for the small taper correction will overpredict the pressure drop to 130–175 psi, for taper angles between 1° and 3°. Naturally, the approximate leading-order solution suggests that these differences become more significant in larger motors for which the constant velocity criterion is not violated. However, using only the leading-order solution to approximate the percent overprediction can result in exaggerated error estimations. With the addition of the first-order correction, it is observed in Fig. 6(b) that the percent over-prediction decreases by approximately 10% to 12%, yielding a maximum percent overprediction of about 63%. The error in predicting the pressure drop without accounting for wall taper propagates along the midsection plane. As the gases approach the aft end of the motor, the pressure drop can be over-predicted by as much as 38% to 63% for taper angles between 1° and 3°.

The information disclosed in Fig. 6 illustrates the dissimilarities in the pressure drops in tapered and parallel chambers. There are obvious implications associated with ignoring the effect of the taper in ballistic analyses. To that end, one can conclude with certainty that the incorporation of taper in some analyses is necessary to prevent overprediction of pressure drop.

Observing the numerical pressure approximation [shown in Fig. 6(c)], it is clear that at larger taper angles and longer tapered domains, the numerical and analytical solutions begin to deviate. Any deviation between the analytical and numerical cases can be partly attributed to neglecting the transverse pressure effects in the analytical solutions. Since the half-height and the radius increase with axial distance, the transverse terms seem to become somewhat more significant farther away from the head end of the motor. As a result, there is a larger overall transverse contribution to the spatial variation of the pressure over the length of the chamber. Although the higher-order analytical expression accounts for the axial derivatives as well as the transverse expansion, the effects of the constant wall distance assumption begin to appear in long tapered domains. This can also cause deviations to build up between the numerical and analytical solutions.

The analytical solution seems to consistently reproduce the results provided by the numerical model. Furthermore, one may recall that the level of precision is governed by the relationship between the asymptotic limit and the mean velocity of the gases. For tapered domains that do not satisfy the relationship prescribed by the asymptotic limit, one discerns increasing deviations between the numerical and analytical solutions.

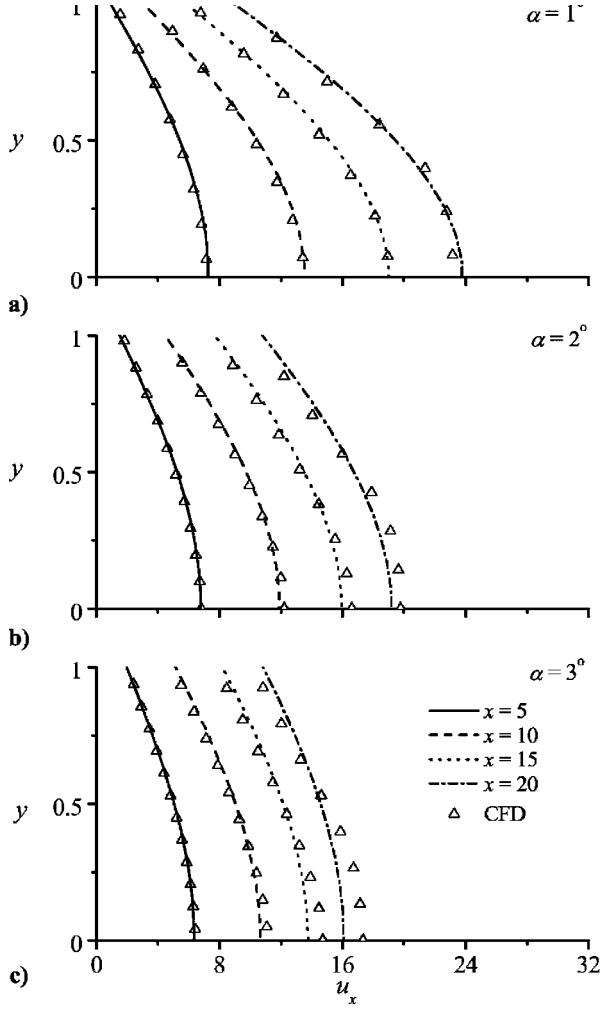

FIG. 7. Numerical versus analytical comparison of slab burner velocity profiles at various locations.

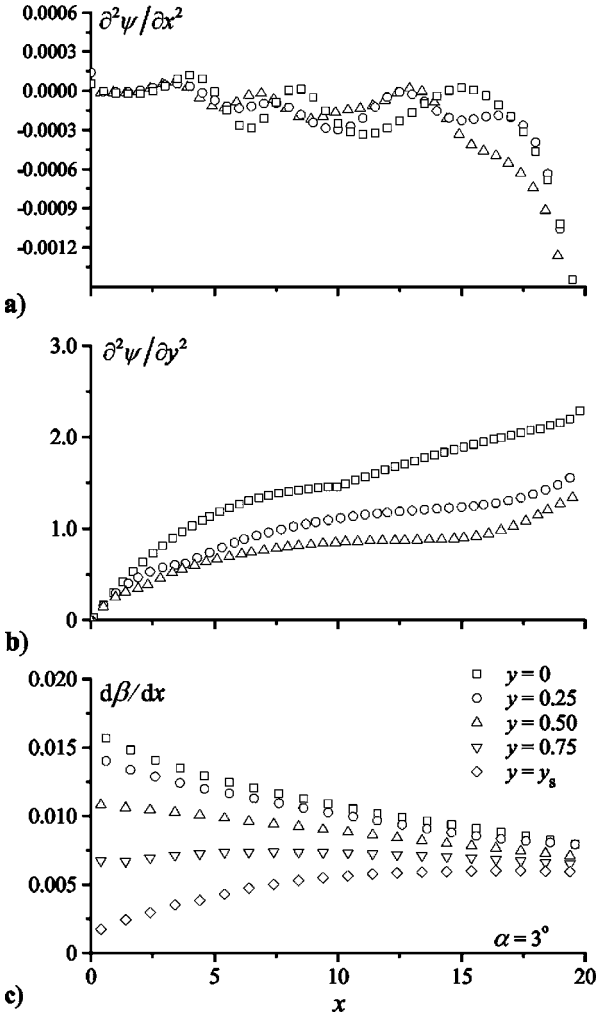

FIG. 8. Computed derivatives shown at several taper angles.

B. Axial velocity

Earlier y_s was treated as a constant during the evaluation of the axial and transverse velocity components. By doing so, it was expected that error would be introduced in the solution. Neglecting the axial variation in chamber half-height, it is clear from Fig. 7 that the axial profiles given by the analytical solution for the slab burner tend to slightly undershoot the numerical solution with increasing axial distance. In fact, the discrepancy becomes more appreciable further down the motor chamber and may become non-negligible in very long slab motors.

One should also note that the analytical solutions shown in Fig. 7 include higher-order corrections. Neglecting these higher-order terms leads to a grossly underpredicted maximum velocity. Again, this suggests that the leading-order solution lacks sufficient flow information and that the higher-order terms appear to be a requisite for accurate solutions in long chambers with large taper angles (i.e., motors with $L \geqslant 4$ and $\alpha \geqslant 2$). The higher-order corrections seem to slowly suppress the error introduced by neglecting the axial variation of the half-height. Nonetheless, Fig. 7 displays rather good agreement between the analytical and numerical solutions.

C. Axial derivatives

The magnitudes of the second-order axial derivatives of streamfunction have been extracted from the numerical solution and quantified along the midsection plane. The second-order transverse derivatives were also obtained to serve as a basis for comparison. From Fig. 8(a), it may be observed that the magnitudes appear to oscillate (as a result of symmetry). More importantly, they remain approximately of $O(10^{-4})$ down the length of the chamber. In contrast, the transverse derivatives ($\partial^2\psi/\partial y^2$) shown in Fig. 8(b) exhibit magnitudes of $O(1)$.

Considering that the axial derivatives are smaller than their transverse counterparts, it may be stated that our numerical results confirm the scaling analysis that justified their dismissal from the analytical formulation.

In the same vein, it is seen in Fig. 8(c) that the magnitudes of the axial derivatives for the velocity ratio are small enough that they would have no appreciable effect on the analytical solution. Here too, the numerical results corroborate the original assumption lurking behind their dismissal. The plot shows the axial variation of $d\beta/dx$ at several transverse locations for $\alpha = 3°$. From the figure, it can be seen that the axial variation of each derivative dictates the shape of the

velocity profile. For example, at $y=y_s$, the axial derivative slowly increases. One may recall that the velocity profile must adjust itself at each axial location to satisfy the no-slip requirement at the tapered surface. Bearing this in mind, it can be inferred that the rate of change at the wall must increase due to the increased axial variation as the gases propagate downstream. Along the midsection, one may notice that the derivative is decreasing. Essentially, this can be ascribed to the depreciation rate of the maximum velocity in the axial direction. From a physical standpoint, this must occur in order to satisfy mass conservation. The increasing rate of change at the wall works in conjunction with the decreasing rate of change along the midsection plane to force the profile to slowly relinquish its transverse component with increasing axial distance. Hence, for sufficiently long tapered domains, the profile may evolve into a near constant shape over the cross section perpendicular to flow. As for the intermediate transverse values, the derivatives exhibit little axial variation being that they are quantified at or near the core.

VII. ERROR ANALYSIS AND LIMITATIONS

For practical applications of the analytical solutions at increasing orders, one may be concerned with their parametric limitations. Previously, such limitations were explored by analytically predicting the behavior of the gases at an infinite distance away from the head end. The results of this inquiry suggest that some relationships, guided by mass conservation, must be maintained between the geometric parameters. The relationship can be expressed as

$$\alpha(L_0+\bar{x})/h_0 \leqslant 1. \tag{84}$$

Equation (84) was obtained using the mean value of the velocity as opposed to the maximum velocity based on Eqs. (19) and (20). In order to determine a maximum range for which the analytical solution remains applicable, one may calculate the maximum relative error between asymptotic predictions and numerical solutions. To do so, it is expedient to examine the asymptotic limit where the velocities in each chamber are at their maximum values, specifically, by comparing the maximum velocities predicted by numerics versus asymptotics. For the nontapered segments, the relation between maximum and mean velocities can be easily found to be

$$u_{\max} = \tfrac{1}{2}\pi u_{\mathrm{m}}. \tag{85}$$

By translating this result to the maximum velocity, the criteria that establish the upper limit of the solution domain may be extrapolated. One finds

$$\frac{\alpha(L_0+\bar{x})}{h_0} \leqslant \frac{2}{\pi}. \tag{86}$$

Equation (86) can now be solved for $L_0=0$ to obtain the maximum *conservative* domain aspect ratio for a given taper angle. One gets

$$x_{\mathrm{cons}} = 2/(\alpha\pi), \tag{87}$$

where $x_{\mathrm{cons}}=\bar{x}/h_0$. It is our observation that, as long as $x \leqslant x_{\mathrm{cons}}$, the percent error between numerics and asymptotics remains less than 1%. The conservative range represents a domain of asymptotic validity in which the accrued error is virtually insignificant. By requiring a minimum chamber aspect ratio of 8 (lest edge effects become important), the maximum conservative taper angle for which an asymptotic solution would exhibit a smaller than 1% error can be calculated from Eq. (87). One finds the maximum conservative taper angle to be 9°. Thus, for the slab burner, a suitable range of tapers would be $0° < \alpha \leqslant 9°$.

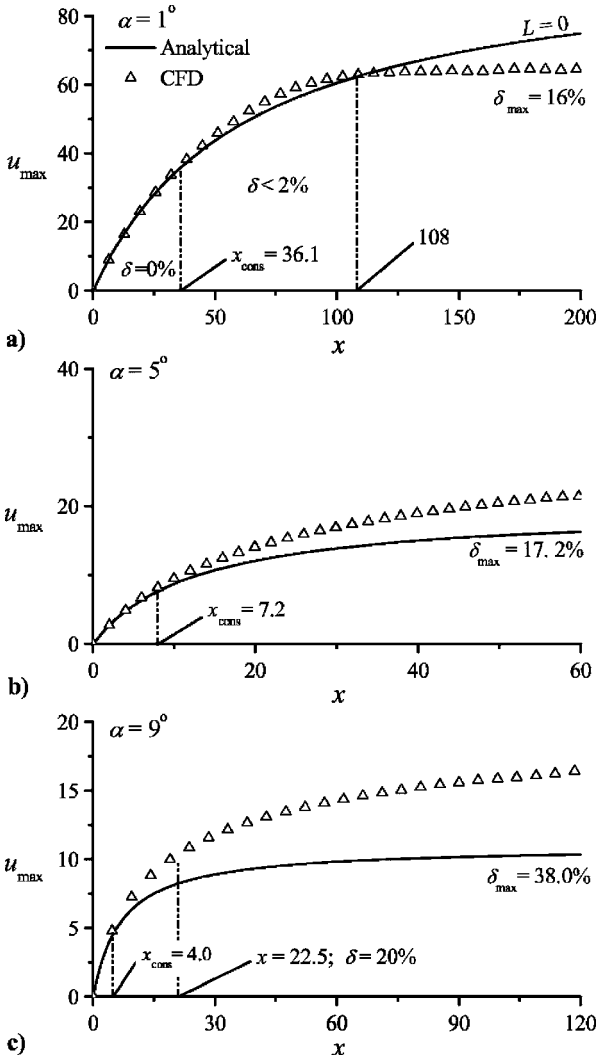

FIG. 9. Numerical and analytical velocities shown at several taper angles. Note that up to x_{cons}, the relative error in the asymptotic expressions is nearly insignificant.

In Fig. 9, the numerical and analytical maximum velocities are plotted at several taper angles. Overall, the figures indicate that within the maximum, *conservative* domain specified by Eq. (87), there is virtually no noticeable deviation between the numerical and analytical solutions (the error remains less than 1%). The issue is, however, with the behavior of the fluid once it exits the domain. At this juncture, one must be concerned with the maximum deviation between the numerical and analytical cases outside of the conservative domain. Here, we choose the maximum allowable percent deviation to be 20% in order to define a longer *approximate* range. In Fig. 9, the numerical and analytical velocities

are shown for extreme values of the taper angle α.

Note that, in Fig. 9(a), we show the maximum velocities corresponding to $\alpha=1°$. Since $x_{cons}=36.1$, it may be noted that as long as $0\leqslant x\leqslant 36.1$, there is virtually no deviation from the numerical solution. In the range $36.1\leqslant x\leqslant 108$, deviations of 1%–2% are observed. For x values greater than 108, the percent deviation undergoes a gradual increase until it reaches a maximum of 16% at $x=200$.

Figure 9(c) illustrates the behavior of the numerical and analytical solutions at $\alpha=9°$. Comparing Fig. 9(a) to Fig. 9(c), it is clear that the conservative domain decreases with an increase in taper angle. Hence, the conservative range for 0%–1% deviation reduces to $0<x\leqslant 4$ (here, $x_{cons}=4$). For the range $4<x\leqslant 22.5$, the percent deviation increases to 20%, which is the maximum allowable error from an engineering perspective. Figure 9(b) constitutes an intermediate case in which $x_{cons}=7.2$. Note that even at the end of the domain ($x=60$), the error remains under 20%.

VIII. CONCLUSIONS

In this work, we have presented an approximate solution for the mean flowfield of a slab rocket motor with tapered walls. Our results support Clayton's approach in which the relationship between the axial pressure gradient and surface vorticity was first explored.[10] Although the distance from the axis to the simulated burning surface varies with axial distance, it is assumed constant in the evaluation of key fluid dynamical quantities such as the velocity, vorticity, and most notably, the pressure drop.

En route to an expression that characterizes the chamber pressure, multiple operations (differentiations and integrations) have been performed with the assumption that the distance from the midsection plane is constant, because its variation appears at $O(\sin\alpha)$. This has prompted a search for a higher-order correction that would inevitably recover the accuracy lost from this restrictive approximation. Based on the results, the higher-order corrections seem to adequately compensate for the assumption of axial independence of the half-height of the slab burner. In addition, the higher-order corrections help to recover contributions due to the second-order axial derivative of the streamfunction as well as the transverse expansion and corresponding flow deceleration.

In summary, we have shown that the pressure drop is overpredicted if Taylor's mean flowfield is applied to chambers with tapered walls. Our results suggest the need to modify ballistic codes that predict and characterize bulk gas motion to the extent of accommodating taper effects. It may be worth mentioning that accurate matching of both the numerical and analytical solutions requires that the motor parameters be chosen within the specified mean flow asymptotic limits, satisfying the relation given by Eq. (20). One shortcoming in the higher-order analytical solution is its algebraic complexity, albeit simple to implement and evaluate. While the leading-order solution can be expressed concisely, it is of marginal accuracy except for motors with short tapered domains and very small taper angles. Better precision can be achieved when the higher-order corrections are added; in this event the total number of terms required to virtually reproduce the numerical predictions can be anywhere from 6 to 20, depending on the desired accuracy.

ACKNOWLEDGMENTS

This project is partially funded by the National Science Foundation through Grant No. CMS-0353518. For his valuable comments and suggestions, the authors are indebted to Dr. Curtis D. Clayton, Propulsion Lead, Missile Defense Target Vehicles, Lockheed Martin Space Systems Company.

[1] F. E. C. Culick, "Rotational axisymmetric mean flow and damping of acoustic waves in a solid propellant rocket," AIAA J. **4**, 1462 (1966).
[2] J. Majdalani, G. A. Flandro, and S. R. Fischbach, "Some rotational corrections to the acoustic energy equation in injection-driven enclosures," Phys. Fluids **17**, 074102 (2005).
[3] G. A. Flandro, J. Majdalani, and J. C. French, "Incorporation of nonlinear capabilities in the standard stability prediction program," AIAA Paper No. 2004–4182, Fort Lauderdale, FL, 2004.
[4] J. Majdalani and W. K. Van Moorhem, "Improved time-dependent flowfield solution for solid rocket motors," AIAA J. **36**, 241 (1998).
[5] J. Majdalani and W. K. Van Moorhem, "Laminar cold-flow model for the internal gas dynamics of a slab rocket motor," Aerosp. Sci. Technol. **5**, 193 (2001).
[6] J. Majdalani, "Physicality of core flow models in rocket motors," J. Propul. Power **19**, 156 (2003).
[7] J. Majdalani and G. A. Flandro, "The oscillatory pipe flow with arbitrary wall injection," Proc. R. Soc. London, Ser. A **458**, 1621 (2002).
[8] J. Majdalani and W. K. Van Moorhem, "The unsteady boundary layer in solid rocket motors," AIAA Paper No. 95–2731, San Diego, CA, 1995.
[9] D. E. Coats and S. S. Dunn, "Improved motor stability predictions for 3D grains using the SPP code," AIAA Paper No. 97–33251, Seattle, WA, 1997.
[10] C. D. Clayton, "Flowfields in solid rocket motors with tapered bores," AIAA Paper No. 96–2643, 1996.
[11] G. I. Taylor, "Fluid flow in regions bounded by porous surfaces," Proc. R. Soc. London, Ser. A **234**, 456 (1956).
[12] S. W. Yuan and A. B. Finkelstein, "Laminar pipe flow with injection and suction through a porous wall," J. Appl. Mech. **78**, 719 (1956).
[13] S. W. Yuan and A. B. Finkelstein, "Heat transfer in laminar pipe flow with uniform coolant injection," Jet Propul. **28**, 178 (1958).
[14] R. M. Terrill and G. M. Shrestha, "Laminar flow through channels with porous walls and with an applied transverse magnetic field," Appl. Sci. Res., Sect. A **11**, 134 (1965).
[15] J. Majdalani, A. B. Vyas, and G. A. Flandro, "Higher mean-flow approximation for a solid rocket motor with radially regressing walls," AIAA J. **40**, 1780 (2002).
[16] C. Zhou and J. Majdalani, "Improved mean flow solution for slab rocket motors with regressing walls," J. Propul. Power **18**, 703 (2002).
[17] T. Mu-Kuan and L. Tong-Miin, "Fiber optic LDV study of the non-uniform, injection induced flow in a 2-D, divergent, porous-walled channel," J. Chin. Soc. Mech. Eng. **11**, 414 (1990).
[18] O. C. Sams, J. Majdalani, and G. A. Flandro, "Higher flowfield approximations for solid rocket motors with tapered bores," AIAA Paper No. 2004–4051, Fort Lauderdale, FL, 2004.
[19] R. S. Brown, A. M. Blackner, P. G. Willoughby, and R. Dunlap, "Coupling between acoustic velocity oscillations and solid propellant combustion," J. Propul. Power **2**, 428 (1986).
[20] R. S. Brown, J. E. Erickson, and W. R. Babcock, "Measuring the combustion response of a forced oscillation method," AIAA J. **12**, 1502 (1974).
[21] R. Dunlap, A. M. Blackner, R. C. Waugh, R. S. Brown, and P. G. Willoughby, "Internal flow field studies in a simulated cylindrical port rocket chamber," J. Propul. Power **6**, 690 (1990).
[22] R. Dunlap, P. G. Willoughby, and R. W. Hermsen, "Flowfield in the combustion chamber of a solid propellant rocket motor," AIAA J. **12**, 1440 (1974).
[23] W.-W. Chu, V. Yang, and J. Majdalani, "Premixed flame response to acoustic waves in a porous-walled chamber with surface mass injection," Combust. Flame **133**, 359 (2003).
[24] A. B. Vyas, J. Majdalani, and V. Yang, "Estimation of the laminar premixed flame temperature and velocity in injection-driven combustion chambers," Combust. Flame **133**, 371 (2003).